New method to determine equivalent black carbon mass size distribution

Weilun Zhao[1], Gang Zhao[2], Ying Li[3,4], Song Guo[2], Nan Ma[5], Lizi Tang[2], Zirui Zhang[2], Chunsheng Zhao[1]

[1]Department of Atmospheric and Oceanic Sciences, School of Physics, Peking University, Beijing 100871, China

[2]State Key Joint Laboratory of Environmental Simulation and Pollution Control, College of Environmental Sciences and Engineering, Peking University, Beijing 100871, China

[3]Department of Ocean Science and Engineering, Southern University of Science and Technology, Shenzhen 518055, China

[4]Southern Marine Science and Engineering Guangdong Laboratory, Guangzhou 511458, China

[5]Institute for Environmental and Climate Research, Jinan University, Guangzhou 511443, China

Correspondence to: Chunsheng Zhao (zcs@pku.edu.cn)

Abstract. Black carbon (BC) is an important atmospheric component with strong light absorption. Many attempts have been made to measure BC mass size distribution (BCMSD) for its significant impact on climate and public health. Larger-coverage BCMSD, ranging from upper submicron to larger than 1 μm, contributes to substantial proportion of total BC mass and absorption. However, current time resolution of larger-coverage BCMSD measurement was limited to 1 day, which was insufficient to characterize variation of larger-coverage BCMSD. In this study, a new method to determine equivalent BCMSD (eBCMSD) was proposed from size-resolved absorption coefficient measured by an aerodynamic aerosol classifier in tandem with an aethalometer. The proposed method could measure larger-coverage eBCMSD with time resolution as high as 1 hour and was validated by comparing the measurement results with refractory BCMSD (rBCMSD) measured by a differential mobility analyzer in tandem with a single particle soot photometer (DMA – SP2) for particle size larger than 300 nm during a field measurement in Yangtze River Delta. Bulk refractory BC mass concentration ($m_{rBC,bulk}$) by DMA – SP2 was underestimated by 33 % compared to bulk equivalent BC mass concentration ($m_{eBC,bulk}$) by this method because of the limited size range of measurement for DMA – SP2. Uncertainty analysis of this method was performed with respect to mass absorption cross-section (MAC), transfer function inversion, number fraction of BC-containing particle and instrumental noise. The results indicated that MAC was the main uncertainty source, leading to $m_{eBC,bulk}$ varied from – 20 % to 28 %. With the advanatage of wide size coverage up to 1.5 μm, high time resolution, easy operation and low cost, this method is expected to have wide applications in field measurement for better estimating radiative properties and climate effects of BC.

1 Introduction

Atmospheric black carbon (BC) is emitted through incomplete combustion of carbon-based fuels (Bond, 2001), such as biomass burning and fossil fuel combustion (Bond et al., 2004). BC warms atmosphere and is considered the third important light absorber in the climate system after CO_2 and CH_4 (Bond et al., 2013). BC can induce the respiratory and cardiovascular disease through inhalation (Highwood and Kinnersley, 2006). Plenty of studies have been devoted to BC for its significant impact on the climate and public health.

Bulk BC mass concentration ($m_{BC,bulk}$) is one of the essential parameters for modeling because radiative transfer models calculate BC absorption from $m_{BC,bulk}$ (Bond et al., 2013). A great deal of research has been dedicated to $m_{BC,bulk}$ measurement for both model assimilation and environmental monitoring (Castagna et al., 2019;Helin et al., 2018;Ran et al., 2016). A recent study indicated that the radiative effect of BC was extremely sensitive to its particle size (Matsui et al., 2018). Zhao et al. (2019) further revealed that the variation of BC mass size distribution (BCMSD), namely size-resolved BC mass concentration ($m_{BC,size\text{-}resolved}$), led to substantial changes in the radiative effect of BC based on field measurement, highlighting the importance of BCMSD on modeling the radiative effect of BC rather than simply $m_{BC,bulk}$. The size of BC affects the deposition rate of BC to the lung (Highwood and Kinnersley, 2006), indicating that BCMSD is closely related to health. In the ambient environment, BCMSD is influenced by emission sources. For instance, BCMSD of fossil fuel combustion differs obviously from that of biomass burning (Schwarz et al., 2008), implying that BCMSD is one of the characteristics of emission source. The temporal variation of BCMSD can reflect the atmospheric aging of BC, during which BC undergoes remarkable change in size, accompanied by dramatical variation of BC optical properties (Zhang et al., 2008). Therefore, reliable measurement and understanding of BCMSD are highly necessary for estimating the impact of BC on both the earth energy budget and public health (Moosmuller et al., 2009).

Quite a few efforts were made to measure BCMSD. The single-particle soot photometer (SP2) was developed using laser-induced incandescence (Schwarz et al., 2006), which measured refractory BCMSD (rBCMSD, Petzold et al. (2013)) on a single-particle level. The soot particle aerosol mass spectrometer (SP-AMS) combined laser-induced incandescence and mass spectroscopy, which could determine not only rBCMSD but also the chemical composition of BC-containing particles (Onasch et al., 2012). The SP2 and SP-AMS techniques were characterized by high time resolution and high accuracy, but high cost and complicated maintenance, as a result, not widely applied for routine measurement. A more convenient solution was required for wider and better characterization of BCMSD in different regions and emission sources. Elemental carbon mass size distribution (ECMSD, Petzold et al. (2013)) could be sampled by multi-stage cascade impactor (Viidanoja et al., 2002) combined with off-line analysis, such as thermo/optical organic carbon/elemental carbon method (Chow et al., 2001). ECMSD sampled by multi-stage cascade impactor had wide size coverage, but low time resolution, usually from 24 hours (Soto-Garcia et al., 2011) to 48 hours (Guo, 2015), which was too low to resolve aging of BC. Differential mobility analyzer (DMA) in tandem with filter-based instrument (Hansen et al., 1984), for instance, micro-aethalometer (MA) (Ning et al., 2013) and particle soot absorption photometer (PSAP) (Tunved et al., 2021), was used to determine equivalent BCMSD (eBCMSD, Petzold et al. (2013)) with higher time resolution up to 2 hours (Zhao et al., 2021b). However, the multiple-charge correction and low flow rate of DMA imposed restrictions on the accuracy of the measured eBCMSD. The measured size range of DMA was limited to less than about 700 nm, resulting in incomplete measured eBCMSD. Current measurement of larger-coverage BCMSD, ranging from upper submicron to larger than 1 μm, was limited in time resolution. Characteristics of larger-coverage BCMSD during atmospheric aging was still unclear. Wang et al. (2022) showed that BC larger than 1 μm could contribute to as large as 50% of $m_{BC,bulk}$, highlighting the importance of larger-coverage BCMSD. Therefore, it was imperative to measure larger-coverage BCMSD with higher time resolution.

In this study, a new method to determine eBCMSD was proposed using size-resolved absorption coefficient ($\sigma_{ab,size\text{-}resolved}$) measured by an aerodynamic aerosol classifier (AAC, Cambustion, UK, Tavakoli and Olfert (2013)) in tandem with an aethalometer (model AE33, Magee, USA, Drinovec et al. (2015)), combined with size-resolved number concentration ($N_{size\text{-}resolved}$), simultaneously measured by scanning mobility particle sizer (SMPS, TSI, USA) and an aerodynamic particle sizer (APS, TSI, USA). The proposed method for determining eBCMSD overcame the disadvantages and weighed the advantages of the above-mentioned methods, characterized by high cost-effectiveness, easy and convenient maintenance, high time resolution to 1 hour, and wide size range to up to 1.5 μm. The proposed method was validated in a field measurement in the Yangtze River Delta and the uncertainty study was carried out based on the measured data.

2 Methods

2.1 Instrumental setup

Figure 1 illustrated the instrumental setup developed in this study, which could be split into two parts, namely the measurement setup and the validation setup. Ambient aerosol particles were drawn througth a PM_{10} inlet (16.67 L min^{-1}) and were dried to relative humidity less than 30 % by silica gel diffusion drier beforehand. An advanced flow splitter were used to split aerosol laden flow into different instruments for isokinetic sampling. For the measurement setup, AAC in tandem with AE33 (AAC – AE33) measured $\sigma_{ab,size\text{-}resolved}$ at a flow rate of 3 L min^{-1}. Since eBCMSD of larger size coverage was mainly focused in this study, AAC was set to scan 12 particle sizes (D_p) logarithmically equally spaced from 200 nm to 1500 nm and smaller size was not scanned. Each size was scanned for 5 minutes and 1 hour was required for a complete cycle. It should be noted that D_p was aerodynamic size in this study. Mobility size related to DMA was converted to aerodynamic size assuming an effective density of 1.3 g cm^{-3} (Zhao et al., 2019;DeCarlo et al., 2005). AE33 measured absorption coefficient (σ_{ab}) at 7 wavelengths from 370 nm to 950 nm (Drinovec et al., 2015), at which 880 nm was adopted in this study because BC dominated particle absorption at 880 nm (Ramachandran and Rajesh, 2007). SMPS and APS measured $N_{size\text{-}resolved}$ for D_p less than and greater than about 800 nm at a flow rate of 0.3 L min^{-1} and 5 L min^{-1}, respectively.

For validation system, the tandem array of Neutralizer, DMA and SP2 (DMA – SP2) measured rBCMSD ($rBCMSD_{DMA\text{-}SP2}$) at a flow rate of 0.12 L min^{-1} for purpose of comparing with eBCMSD determined by the proposed method ($eBCMSD_{AAC\text{-}AE33}$). Another AE33 measured bulk absorption coefficient ($\sigma_{ab,bulk}$) simultaneously at a flow rate of 2 L min^{-1} for closure study with $\sigma_{ab,size\text{-}resolved}$.

2.1.1 AE33

The principle of obtaining σ_{ab} was well developed for aethalometer (Hansen et al., 1984) and described here in brief. Ambient aerosol particles were drawn into an aethalometer at a flow rate F and collected on an area S of a filter. A light source illuminated the filter. The transmitted light signal was denoted as I (I_0) for the light which passed through the particle-laden (particle-free) part of the filter. Light attenuation was defined as

$$\mathrm{ATN} = -100 \cdot \ln\left(\frac{I}{I_0}\right). \quad (1)$$

ATN increased with decreasing I as aerosol particles were loaded on the filter continuously. Therefore, ATN reflected aerosol loading on the filter. If ATN increased ΔATN during time interval Δt, then attenuation coefficient was defined as

$$\sigma_{\mathrm{ATN}} = \frac{S}{100 \cdot F} \cdot \frac{\Delta \mathrm{ATN}}{\Delta t}. \quad (2)$$

The light attenuation was caused by not only particle absorption, but also scattering by particle and filter matrix. A scattering parameter C_f was introduced to extract σ_{ab} from σ_{ATN}:

$$\sigma_{\mathrm{ab}} = \frac{\sigma_{\mathrm{ATN}}}{C_f}, \quad (3)$$

where C_f was set as 2.9 (Zhao et al., 2020b) in this study. Nonlinearity, termed loading effect, became more and more significant with increasing aerosol loading, namely for the same increase in aerosol loading, the corresponding increase in ATN was smaller for heavier aerosol loading. The "dual-spot" technique (Drinovec et al., 2015) was proposed to correct the loading effect for AE33 and was used in this study. The σ_{ab} measured by AE33 at given particle size selected by AAC was termed binned σ_{ab} ($\sigma_{\mathrm{ab,binned}}$) in this study to differentiate from $\sigma_{\mathrm{ab,bulk}}$.

2.1.2 AAC

The principle of AAC was illustrated detailedly by Tavakoli and Olfert (2013) and was introduced here concisely. The setup of AAC could be simplified to two coaxial cylinders, where the inner radius, outer radius and length was denoted as r_{i}, r_{o} and L. Polydisperse particles flowed into the space between the inner cylinder and outer cylinder from one end of the inner cylinder at a flow rate of Q_{sample}. Meawhile, Particle free sheath flow streamed in the space between the inner cylinder and outer cylinder in the direction of the axis of the coaxial cylinders at a flow rate of Q_{sheath}. The sheath flow carried the particles along the coaxial cylinders. At the same time, the two coaxial cylinders rotated with respect to their axis at a rotational speed of ω. Therefore, the particles was migrated outwards across the sheath flow by the centrifugal force acting on them. Relaxation time (τ) was defined as

$$\tau = \frac{C_{\mathrm{c}}(D_{\mathrm{p}})\rho_0 D_{\mathrm{p}}^2}{18\mu}, \quad (4)$$

where $C_{\mathrm{c}}(D_{\mathrm{p}})$ was the Cunningham slip correction factor as a function of D_{p} (Kim et al., 2005), ρ_0 = 1 g cm^{-3} was the reference density and μ was the gas viscosity. It could be seen that τ was directly related to D_{p}. Dynamic analysis proved that only particles with certain relaxation time τ, and hence certain D_{p}, could migrate to another end of outer cylinder and emerge as monodisperse flow. τ was related to parameters of AAC by

$$\tau = \frac{2Q_{\mathrm{sheath}}}{\pi\omega^2(r_{\mathrm{i}}+r_{\mathrm{o}})^2 L}. \quad (5)$$

Therefore, by changing ω and Q_{sheath}, monodisperse particles of desired D_{p} could be selected by AAC. Unlike DMA, particles did not need to be charged before entering AAC. Consequently, the transmission efficiency (λ_Ω) of AAC was about 4 times higher than that of DMA and multi-charge correction was not required for AE33 (Johnson et al., 2018).

2.1.3 DMA – SP2

The reason why DMA – SP2 was used rather than SP2 alone was that D_{p} could be directly measured by DMA. If SP2 was used

alone, D_p was calculated from Mie theory with assumed inputs (Taylor et al., 2015). The detail of DMA – SP2 was described by Zhao et al. (2021a) and presented here concisely. The incandescence high gain channel and incandescence low gain channel of SP2 were calibrated by Aquadag soot particles with effective density of 1.8 g cm^{-3} before measurement. DMA was set to scan D_p from 15 nm to 780 nm with 56 bins at time resolution of 5 min. D_p and time resolution of measured $rBCMSD_{DMA\text{-}SP2}$ was interpolated and time-averaged to that of $eBCMSD_{AAC\text{-}AE33}$ for comparison. It should be noted that 780 nm, the upper D_p limit scanned by DMA, lied between 720 nm and 865 nm, two of the scanned D_ps by AAC. Therefore, upper D_p limit of the interplolated $rBCMSD_{DMA\text{-}SP2}$ was 720 nm in this study. Similarly, the lower D_p limit of the interplolated $rBCMSD_{DMA\text{-}SP2}$ was 200 nm. According to Zhao et al. (2020a), DMA – SP2 could not detect particle less than about 200 nm, consistent with the lower limit of D_p in this study.

The number distribution of BC-containing particle measured by DMA – SP2 could be presented as a bivariate function $\frac{\partial^2 N_{BC}}{\partial \log D_p \partial \log D_c}$, where N_{BC} was the number concentration of BC-containing particle, and D_c was the core diameter assuming that BC-containing particle had a core-shell geometry. It should be pointed out that asphericity of rBC was not considered in this study. D_c was logarithmically equally distributed from 78 nm to 560 nm with 29 bins. At a given D_c bin, the number distribution of BC-containing particle could be considered as a univariate function $\frac{dN_{BC}}{d\log D_p}$. The multiple charging correction of 1-dimensional size distribution was developed by Knutson and Whitby (1975), which was adopted to correct $\frac{dN_{BC}}{d\log D_p}$. By correcting $\frac{dN_{BC}}{d\log D_p}$ at each D_c bin, multiple charging correction of $\frac{\partial^2 N_{BC}}{\partial \log D_p \partial \log D_c}$ was achieved.

2.2 Field measurement

The proposed method was applied to a field measurement in Changzhou, Jiangsu Province, China (119°36′E, 31°43′N), located in the Yangtze River Delta, from May 17th to June 3rd in 2021. Changzhou was between two megacities, about 187 km to the northwest of Shanghai and about 82 km to the southeast of Nanjing, as shown in Fig. S1a. The area between the Shanghai and Nanjing underwent serious environmental pollution in the past few decades with the development of industrialization and urbanization. As shown in Fig. S1b, the pollution condition of Changzhou was overall representative of the regional background pollution in the Yangtze River Delta.

2.3 Size-resolved calculations

2.3.1 $\sigma_{ab,size\text{-}resolved}$

Tavakoli and Olfert (2013) formulated the ideal theoretical model for AAC transfer function inversion, which was adopted by this study to derive $\sigma_{ab,size\text{-}resolved}$ from $\sigma_{ab,binned}$ and presented here in short. The $\sigma_{ab,size\text{-}resolved}$ was given by

$$\sigma_{ab,size-resolved} = \frac{d\sigma_{ab}}{d\log D_p} = \frac{\ln(10)}{\frac{d\log D_p}{d\log \tau}\cdot\beta^*} \cdot \sigma_{ab,binned}, \quad (6)$$

where β^* was related to the ratio of Q_{sheath} to Q_{sample}, $R_t = Q_{sheath}/Q_{sample} = 1/\beta$, through

$$\beta^* = \left(1+\frac{1}{\beta}\right)\ln(1+\beta) - \left(1-\frac{1}{\beta}\right)\ln(1-\beta). \quad (7)$$

Johnson et al. (2018) corrected the ideal inversion formula (6) to take particle loss and spectral broadening into account by replacing

β^* with a nonideal β^*_{NI}:

$$\beta^*_{NI} = \lambda_\Omega \mu_\Omega \left[\ln\left(\frac{1+\beta/\mu_\Omega}{1-\beta/\mu_\Omega}\right) + \frac{\mu_\Omega}{\beta} \ln\left(1-\left(\frac{\beta}{\mu_\Omega}\right)^2\right)\right], \quad (8)$$

where μ_Ω was the spectral broadening factor. Both λ_Ω and μ_Ω were dependent on D_p as well as flow, and discussed in detail in Sect. 4.2.

2.3.2 eBCMSD$_{AAC\text{-}AE33}$

$\sigma_{ab,size\text{-}resolved}$ could be converted to eBCMSD$_{AAC\text{-}AE33}$ through mass absorption cross-section (MAC) (Bond and Bergstrom, 2006), which was determined based on method proposed by Zhao et al. (2021b). Briefly, a 2-dimensional lookup table of MAC with respect to D_p and D_c was simulated (MAC(D_p, D_c)) by Mie theory assuming a core-shell geometry. At a given size bin centered at D_p, the corresponding σ_{ab} and number concentration (N) at the size bin, denoted as $\sigma_{ab}(D_p)$ and $N(D_p)$, could be derived by $\sigma_{ab,size\text{-}resolved}$ and $N_{size\text{-}resolved}$:

$$\sigma_{ab}(D_p) = \sigma_{ab,size-resolved}(D_p) \cdot \Delta \log D_p, \quad (9)$$

$$N(D_p) = N_{size-resolved}(D_p) \cdot \Delta \log D_p, \quad (10)$$

where $\Delta\log D_p$ was the logarithmic width of the size bin. The number concentration of BC-containing particle at the size bin $N_{BC}(D_p)$ was determined by

$$N_{BC}(D_p) = N(D_p) \cdot f_{BC}, \quad (11)$$

where f_{BC} was the number fraction of BC-containing particle, which was assumed as a fixed value in this study and the uncertainty of the fixed-f_{BC} assumption was discussed in Sect. 4.3. An optimal D_c was found so that calculated σ_{ab} at the size bin, denoted as $\sigma_{ab,calc}(D_p, D_c)$, matched $\sigma_{ab}(D_p)$:

$$\sigma_{ab,calc}(D_p, D_c) = \rho_{BC} \frac{\pi}{6} {D_c}^3 \cdot \mathrm{MAC}(D_p, D_c) \cdot N_{BC}(D_p) = \sigma_{ab}(D_p), \quad (12)$$

where ρ_{BC} was the density of BC, and set as 1.8 g cm^{-3} (Bond and Bergstrom, 2006), consistent with the ρ_{BC} assumption when deriving rBCMSD$_{DMA\text{-}SP2}$. Equivalent BC mass concentration (m_{eBC}) at the size bin, denoted as $m_{eBC}(D_p)$, could be determined by

$$m_{eBC}(D_p) = \frac{\sigma_{ab}(D_p)}{\mathrm{MAC}(D_p, D_c)}, \quad (13)$$

then the eBCMSD$_{AAC\text{-}AE33}$ at D_p, denoted by eBCMSD$_{AAC\text{-}AE33}$(D_p), could be determined by

$$\mathrm{eBCMSD}(D_p) = \frac{m_{eBC}(D_p)}{\Delta \log D_p}. \quad (14)$$

3 Results and discussion

Figure 2 presented the time series of the measurement results. There were 4 pollution episodes during the measurement period: from about 12:00 May 17th to about 00:00 May 20th, from about 00:00 May 21st to about 12:00 May 22nd, from about 00:00 May 24th to about 12:00 May 26th, and from about 12:00 May 28th to about 12:00 May 31st, as shown in Fig. 2a. Both eBCMSD$_{AAC\text{-}AE33}$ (Fig. 2b) and rBCMSD$_{DMA\text{-}SP2}$ (Fig. 2c) recorded the 4 pollution episodes simultaneously with higher BCMSD values than clean episodes. eBCMSD$_{AAC\text{-}AE33}$ and rBCMSD$_{DMA\text{-}SP2}$ were both integrated from 200 nm to 720 nm, which was the D_p range of

measurement for DMA – SP2, and the results were denoted as $m_{\mathrm{eBC,bulk,AAC\text{-}AE33,200\text{-}720}}$ and $m_{\mathrm{rBC,bulk,DMA\text{-}SP2,200\text{-}720}}$, respectively. As shown in Fig. 2a, $m_{\mathrm{eBC,bulk,AAC\text{-}AE33,200\text{-}720}}$ compared well with $m_{\mathrm{rBC,bulk,DMA\text{-}SP2,200\text{-}720}}$ with determination coefficient (R^2), slope (b_1), and intercept (b_0) of 0.8 (accurate to one decimal place), 1.0 and 0.1 μg m^{-3} (Fig. S2a). R^2 of 0.8 and b_1 of 1.0 indicated the proposed method was capable of capturing the variation of $m_{\mathrm{BC,bulk}}$. The mean $m_{\mathrm{eBC,bulk,AAC\text{-}AE33,200\text{-}720}}$ and $m_{\mathrm{rBC,bulk,DMA\text{-}SP2,200\text{-}720}}$ were 0.7 ± 0.4 μg m^{-3} and 0.6 ± 0.3 μg m^{-3}, indicating $m_{\mathrm{eBC,bulk,AAC\text{-}AE33,200\text{-}720}}$ was overall 0.1 μg m^{-3} higher than $m_{\mathrm{rBC,bulk,DMA\text{-}SP2,200\text{-}720}}$, consistent with b_0 of 0.1 μg m^{-3}. The reason for overall discrepancy of 0.1 μg m^{-3} in $m_{\mathrm{BC,bulk,200\text{-}720}}$ might be that DMA – SP2 could not detect rBC with D_c less than about 100 nm (Zhao et al., 2020a), resulting in an underestimated $m_{\mathrm{rBC,bulk,DMA\text{-}SP2,200\text{-}720}}$. $\mathrm{eBCMSD_{AAC\text{-}AE33}}$ was also integrated from 720 nm to 1500 nm, which was the D_p range that DMA – SP2 did not measure, and the result was denoted as $m_{\mathrm{eBC,bulk,AAC\text{-}AE33,720\text{-}1500}}$. $m_{\mathrm{eBC,bulk,AAC\text{-}AE33,720\text{-}1500}}$ was correlated to $m_{\mathrm{rBC,bulk,DMA\text{-}SP2,200\text{-}720}}$ to study whether BCMSD ranging from 720 nm to 1500 nm was connected to that ranging from 200 nm to 720 nm, as shown in Fig. S2b. R^2 decreased to 0.2 between $m_{\mathrm{eBC,bulk,AAC\text{-}AE33,720\text{-}1500}}$ and $m_{\mathrm{rBC,bulk,DMA\text{-}SP2,200\text{-}720}}$, indicating these two size ranges were not well related and both of them needed to be measured exclusively. Observation by transmission electron microscopy showed that these larger BC-containing particles could be coated with massizve materials from secondary processes, or superaggregated BC with fractal BC structure (Wang et al., 2022). The mean $m_{\mathrm{eBC,bulk,AAC\text{-}AE33,720\text{-}1500}}$ was 0.2 ± 0.2 μg m^{-3}, indicating that DMA – SP2 overall underestimated $m_{\mathrm{BC,bulk}}$ for ~ 0.2 μg m^{-3} (~ 33 %) in this field measurement considering that DMA – SP2 did not measure BCMSD larger than 720 nm. Therefore, it was highly necessary to measure BCMSD with wider D_p range for better estimation of $m_{\mathrm{BC,bulk}}$ and deeper understanding of BC evolution in the atmosphere.

Figure 3 exhibited the mean $\mathrm{eBCMSD_{AAC\text{-}AE33}}$ ($\overline{\mathrm{eBCMSD}}_{\mathrm{AAC-AE33}}$) and mean $\mathrm{rBCMSD_{DMA\text{-}SP2}}$ ($\overline{\mathrm{rBCMSD}}_{\mathrm{DMA-SP2}}$) during the field measurement. It could be seen that when D_p was less than about 300 nm, $\overline{\mathrm{eBCMSD}}_{\mathrm{AAC-AE33}}$ was higher than $\overline{\mathrm{rBCMSD}}_{\mathrm{DMA-SP2}}$. The higher $\overline{\mathrm{eBCMSD}}_{\mathrm{AAC-AE33}}$ may be due to particle diffusion at small D_p which was not well corrected by (7) and underestimated MAC. When D_p was greater than 300 nm and less than 720 nm, $\overline{\mathrm{eBCMSD}}_{\mathrm{AAC-AE33}}$ was overall consistent with $\overline{\mathrm{rBCMSD}}_{\mathrm{DMA-SP2}}$. When D_p was larger than 720 nm, where DMA – SP2 did not measure, $\overline{\mathrm{eBCMSD}}_{\mathrm{AAC-AE33}}$ decreased with increasing D_p when D_p less than about 870 nm, and increased with increasing D_p when D_p was larger than 870 nm. In the study by Yu et al. (2010), three modes of BCMSD were identified: the mode peaked at about 400 nm, 1000 nm and 5000 nm, which were termed as condensation mode, droplet mode and coarse mode, respectively. Following the nomenclature proposed by Yu et al. (2010), the increasing (decreasing) $\overline{\mathrm{eBCMSD}}_{\mathrm{AAC-AE33}}$ with increasing D_p for D_p larger (less) than 870 nm signified the lower (upper) end of droplet mode (condensation mode). However, $\overline{\mathrm{rBCMSD}}_{\mathrm{DMA-SP2}}$ only identified condensation mode, which clearly highlighted the necessity to measure BCMSD of wider D_p range for better characterization of BCMSD. Both the proposed method and DMA – SP2 showed that the temporal variation of BCMSD, expressed as standard deviation (std) of BCMSD in Fig. 3, was as large as $\overline{\mathrm{BCMSD}}$, reflecting the complex mechanism in the variability of BCMSD.

4 Uncertainty analysis

Uncertainty analysis was performed with respect to the MAC lookup table, transfer function inversion from $\sigma_{\mathrm{ab,binned}}$ to $\sigma_{\mathrm{ab,size\text{-}}}$

$_{resolved}$, f_{BC} and instrumental noise, respectively. The resulting uncertainty to $eBCMSD_{AAC\text{-}AE33}$ was illustrated in Fig. 4 and to $m_{eBC,bulk,AAC\text{-}AE33,200\text{-}720}$ was shown in table 1. It could be seen from Fig. 4 that the boundary between condensation mode and droplet mode was distinct no matter how the uncertainty sources disturbed $eBCMSD_{AAC\text{-}AE33}$.

4.1 Uncertainty from masss absorption cross-section

According to Zhao et al. (2021b), the variation in refractive index (RI) dominated the uncertainty of the MAC lookup table. Therefore, the uncertainty from the MAC lookup table was analyzed with respect to RI. The real part of RI (Re[RI]) was reported to vary from 1.5 to 2.0 in general (Liu et al., 2018) and the imaginary part of RI (Im[RI]) ranged from 0.5 to 1.1 commonly (Bond and Bergstrom, 2006). Hence, Re[RI] (Im[RI]) was changed from 1.5 (0.5) to 2.0 (1.1) with step increase of 0.01, the resulting mean MAC ($\overline{MAC}$) was the MAC lookup table used in this study (Fig. S3a) and the resulting std divided by the $\overline{MAC}$ was considered as the uncertainty of the MAC lookup table (Fig. S3b). As shown in Fig. S3b, when D_c was larger than about 400 nm, the uncertainty was less than 10% and influenced by both D_p and D_c. However, when D_c was less than 400 nm, the uncertainty increased rapidly with decreasing D_c and was dominated by D_c. The uncertainty increased to larger than 23 % when D_c was less than about 100 nm. When D_p was less than about 300 nm, the uncertainty varied from 14% to 24% with a mean value of 22 %, indicating large uncertainty in $eBCMSD_{AAC\text{-}AE33}$ for D_p less than 300 nm.

The MAC lookup table was replaced with original $\overline{MAC}$ minus its std (-stdMAC) and plus its std (+stdMAC). The resulting MAC lookup tables were taken into the method proposed by Zhao et al. (2021b), and applied to the entire measurement period to study the influence of MAC variation on the $eBCMSD_{AAC\text{-}AE33}$. $\overline{eBCMSD}_{AAC-AE33}$ and mean $eBCMSD_{AAC\text{-}AE33}$ after $\pm$ stdMAC were shown in Fig. 4a. The uncertainty increased with decreasing D_p, and reached to maximum when D_p was less than 300 nm, indicating the $eBCMSD_{AAC\text{-}AE33}$ for D_p less than 300 nm might potentially have nonnegligible uncertainty. The uncertainty in $m_{eBC,bulk,AAC\text{-}AE33,200\text{-}720}$ was from – 20 % (+stdMAC) to + 28 % (-stdMAC), which was the largest among the four uncertainty sources, as shown in Table 1.

4.2 Uncertainty from the transfer function inversion

As stated in Sect. 2.4.1, correction for particle loss and spectral broadening was required when $\sigma_{ab,binned}$ was converted to $\sigma_{ab,size\text{-}resolved}$. λ_Ω was defined to correct particle loss where $\lambda_\Omega = 0$ ($\lambda_\Omega = 1$) stood for total (no) particle loss. The relationships between λ_Ω and D_p as well as Q_{sample}, as shown in Fig. S4a, were well developed (Karlsson and Martinsson, 2003) and consistent with experimental data of AAC (Johnson et al., 2018). Q_{sample} used in this study was 3.0 L min^{-1}. Q_{sample} was changed from – 30 % (2.1 L min^{-1}) to + 30% (3.9 L min^{-1}), and the resulting λ_Ω was used to study the fluctuation of Q_{sample} on λ_Ω. As shown in Fig. S4a, the variation of λ_Ω was less than 0.5 %, which was negligible.

Spectral broadening was caused by small-size particle diffusion as well as disturbance of sheath flow due to complicated rotation fluid dynamics inside AAC and described by μ_Ω where $\mu_\Omega < 1$ ($\mu_\Omega = 1$) was for (no) broadening. Johnson et al. (2018) found that behavior of μ_Ω with respect to D_p ($\mu_\Omega(D_p)$) depended on both Q_{sheath} and Q_{sample}, and parameterized $\mu_\Omega(D_p)$ (Fig. S4b) based on two case studies of (Q_{sheath}, Q_{sample}), namely (3 L min^{-1}, 0.3 L min^{-1}) and (15 L min^{-1}, 1.5 L min^{-1}):

$$\mu_{\Omega,\mathrm{Johnson}}(D_\mathrm{p}) = 0.318 \cdot D_\mathrm{p}^{0.0946}. \quad (15)$$

(Q_{sheath}, Q_{sample}) was (7.5 L min^{-1}, 3 L min^{-1}) in this study, which might lead to uncertainty if $\mu_{\Omega,\mathrm{Johnson}}(D_\mathrm{p})$ was directly used in this study. $\mu_{\Omega,\mathrm{Johnson}}(D_\mathrm{p})$ was varied from – 23 % to + 30 % to study the impact of μ_Ω on $\mathrm{eBCMSD}_{\mathrm{AAC\text{-}AE33}}$. The resulting influence on the $\mathrm{eBCMSD}_{\mathrm{AAC\text{-}AE33}}$ was shown in Fig. 4b. The uncertainty of μ_Ω did not exhibit a significant size dependence. Lower μ_Ω led to lower $\mathrm{eBCMSD}_{\mathrm{AAC\text{-}AE33}}$, and vice versa. The difference in the $m_{\mathrm{eBC,bulk,AAC\text{-}AE33,200\text{-}720}}$ was from – 1% (– 23% of $\mu_{\Omega,\mathrm{Johnson}}$) to + 21% (+ 30% of $\mu_{\Omega,\mathrm{Johnson}}$), implying systematic overestimation of $m_{\mathrm{eBC,bulk,AAC\text{-}AE33,200\text{-}720}}$. Therefore, $\mu_\Omega(D_\mathrm{p}) = 77\%\mu_{\Omega,\mathrm{Johnson}}(D_\mathrm{p})$ was used in this study to offset the bias. The reason for the lower limit of μ_Ω set as – 23 % rather than – 30 % was that $\mathrm{eBCMSD}_{\mathrm{AAC\text{-}AE33}}$ was invalid mathematically when μ_Ω was less than – 23 % under setting of (Q_{sheath}, Q_{sample}) used in this study. It should be pointed out that AAC – AE33 could still determine valid eBCMSD under the condition of $\mu_\Omega(D_\mathrm{p}) < 77\%\mu_{\Omega,\mathrm{Johnson}}(D_\mathrm{p})$ by increasing Q_{sheath}. Q_{sheath} was not changed in this study because desired $\mu_\Omega(D_\mathrm{p})$ parameterization was found at $\mu_\Omega(D_\mathrm{p}) = 77\%\mu_{\Omega,\mathrm{Johnson}}(D_\mathrm{p})$.

$\sigma_{\mathrm{ab,size\text{-}resolved}}$ (Fig. S5b) was integrated and the result, denoted as $\sigma_{\mathrm{ab,bulk,calc}}$ was compared to $\sigma_{\mathrm{ab,bulk}}$. As shown in Fig. S5a, $\sigma_{\mathrm{ab,bulk,calc}}$ was consistent with $\sigma_{\mathrm{ab,bulk}}$. R^2, b_1 and b_0 between $\sigma_{\mathrm{ab,bulk,calc}}$ and $\sigma_{\mathrm{ab,bulk}}$ was 0.9, 1.1, and 0.5 Mm^{-1} (Fig. S6), respectively, which validated conversion from $\sigma_{\mathrm{ab,binned}}$ to $\sigma_{\mathrm{ab,size\text{-}resolved}}$.

4.3 Uncertainty from number fraction of BC-containing particle

BC-containing aerosol particles had complicated mixing states. Even for internally-mixed particles with same D_p, the internal BC cores might have different D_c, which could not be resolved by AAC – AE33. Field measurement (Liu et al., 2010) revealed that f_{BC} varied with time, D_c and D_p. This complexity was simplified to a parameterized fixed value of f_{BC} in this study. A fixed f_{BC} implied that only one D_c value corresponded to a given D_p and the size-resolved number concentration of BC-containing particle was determined by $N_{\mathrm{size\text{-}resolved}}$ times f_{BC}. Zhao et al. (2021b) used f_{BC} value of 0.17 based on SP2 measurement. However, SP2-derived f_{BC} could not represent the bulk f_{BC} over the whole particle size spectrum due to the detection limit of SP2. And different regions might have different f_{BC}. In this study, f_{BC} was varied and the resulting $m_{\mathrm{eBC,bulk,AAC\text{-}AE33,200\text{-}720}}$ was compared with $m_{\mathrm{rBC,bulk,DMA\text{-}SP2,200\text{-}720}}$. f_{BC} was set as 0.35 in this study because b_1 was 1.0 between $m_{\mathrm{eBC,bulk,AAC\text{-}AE33,200\text{-}720}}$ and $m_{\mathrm{rBC,bulk,DMA\text{-}SP2,200\text{-}720}}$ when f_{BC} was 0.35.

f_{BC} was varied from 0.25 (– 30 % of 0.35) to 0.46 (+ 30 % of 0.35) to analyze the influence of f_{BC} on the $\mathrm{eBCMSD}_{\mathrm{AAC\text{-}AE33}}$, as shown in Fig. 4c. $\mathrm{eBCMSD}_{\mathrm{AAC\text{-}AE33}}$ was more influenced around 870 nm. The variation of f_{BC} led to uncertainty of $\pm$3 % in $m_{\mathrm{eBC,bulk,AAC\text{-}AE33,200\text{-}720}}$, indicating that simplification of f_{BC} was a minor uncertainty source compared to MAC and transfer function inversion.

4.4 Uncertainty from instrumental noise

The instrumental noise stemmed from the fluctuation of the light source and flow of AE33, which was reflected as fluctuation in I, I_0 and F, further leading to the fluctuation in ATN, σ_{ATN} and σ_{ab}. The instrumental noise was defined as the std of $\sigma_{\mathrm{ab,binned}}$ and was shown in Fig. S7b. It could be seen that the instrumental noise did not exhibit significant dependence on D_p. Comparing Fig. S7a and Fig. S7b, the instrumental noise was irrelevant to the value of $\sigma_{\mathrm{ab,binned}}$. Figure S7c illustrated that the instrumental noise was also not correlated to $\sigma_{\mathrm{ab,bulk}}$ with R^2, b_1 and b_0 of 0.0, 0.0 and 0.1 Mm^{-1}, respectively, implying that the instrumental noise was not

dependent on the pollution level.

The std of instrumental noise was added to (subtracted from) $\sigma_{ab,binned}$ and the derived $eBCMSD_{AAC-AE33}$ was used to study the influence of instrumental noise on $eBCMSD_{AAC-AE33}$. The mean result was shown in Fig. 4d. $eBCMSD_{AAC-AE33}$ larger than 1000 nm was more influenced by the instrumental noise than $eBCMSD_{AAC-AE33}$ smaller than 500 nm. $\sigma_{ab,binned}$ larger than 1000 nm was relatively small (about 0.3 Mm^{-1}) compared to $\sigma_{ab,binned}$ less than 870 nm (about 0.9 Mm^{-1}). The mean instrumental noise was 0.1 Mm^{-1} and exhibited no significant dependence on D_p. Therefore, $\sigma_{ab,binned}$ larger than 1000 nm was more affected by the instrumental noise, resulting in distinct variation in $eBCMSD_{AAC-AE33}$. The uncertainty in $m_{eBC,bulk,AAC-AE33,200-720}$ was not obvious, which varied from – 2 % to – 1 %, also minor compared to MAC and transfer function inversion.

5 Summary

Knowledge of bulk black carbon (BC) characteristics, such as bulk BC mass concentration ($m_{BC,bulk}$), was very limiting for deeper understanding the influence of BC on radiation and health. BC mass size distribution (BCMSD) was one of the BC microphysical characteristics that could indicate emission source, reflect atmospheric aging and effectively reduce uncertainty related to BC radiative effect. However, current BCMSD measurement ranging from upper micron to larger than 1 μm was insufficient in time resolution and sophisiticated for routine measurement. In this study, a new method to determine equivalent BCMSD (eBCMSD) was proposed characterized by wide size range of measurement up to 1.5 μm, high time resolution up to 1 hour and convenience for extensive measurement. The eBCMSD was retrieved by size-resolved absorption coefficient ($\sigma_{ab,size-resolved}$) measured by an aerodynamic aerosol classifer in tandem with an aethaelometer model AE33 (AAC – AE33), denoted as $eBCMSD_{AAC-AE33}$. Size-resolved number concentration ($N_{size-resolved}$) was measured concurrently by scanning mobility particle sizer (SMPS) and an aerodynamic particle sizer (APS) to model the influence of size on mass absorption cross-section (MAC).

The proposed method was applied to a field measurement in Yangtze River Delta and validated by comparing the refractory BCMSD (rBCMSD) with that measured by an differential mobility analyzer in tandem with a single-particle soot photometer (DMA – SP2), denoted as $rBCMSD_{DMA-SP2}$. The results showed that for particle diameter (D_p) less than 300 nm, $eBCMSD_{AAC-AE33}$ was higher than $rBCMSD_{DMA-SP2}$, which might be caused by underestimated MAC by the method proposed by Zhao et al. (2021b) or incomplete parameterization of spectral broadening of AAC. $eBCMSD_{AAC-AE33}$ was consistent with $rBCMSD_{DMA-SP2}$ for D_p larger than 300 nm. $m_{BC,bulk}$ integrated over the size range that AAC – AE33 and DMA – SP2 both measured (200 nm – 720 nm), denoted as $m_{eBC,bulk,AAC-AE33,200-720}$ and $m_{rBC,bulk,DMA-SP2,200-720}$, compared well with each other with determination coefficient (R^2), slope (b_1), and intercept (b_0) of 0.8, 1.0 and 0.1 μg m^{-3}, respectively. However, DMA – SP2 did not measure D_p larger than 700 nm, leading to 0.2 μg m^{-3} (33 %) underestimation of $m_{BC,bulk}$, highlighting the necessity to measure BCMSD with a wider size range.

Uncertainty analysis was performed with respect to MAC, transfer function inversion, number fraction of BC-containing particle (f_{BC}) and instrumental noise. MAC was the largest uncertainty source, leading to significant uncertainty for D_p less than 300 nm and about 24% uncertainty in $m_{eBC,bulk,AAC-AE33,200-720}$. Transfer function inversion was the second largest uncertainty source, which was induced by incomplete parameterization of spectral broadening. The uncertainty in transfer function inversion led to systematic

overestimation of $m_{eBC,bulk,AAC\text{-}AE33,200\text{-}720}$, which was corrected in this study. Both f_{BC} and instrumental noise were minor uncertainty sources and one order of magnitude less than MAC and transfer function inversion. f_{BC} was simplification of complicated BC mixing states, leading to relatively big uncertainty in eBCMSD at 870 nm, around the boundary between condensation mode and droplet mode. The eBCMSD for D_p larger than 1000 nm was more sensitive to instrumental noise.

Data availability

The measurement data involved in this study are available upon request to the authors.

Author contributions

CZ determined the main goal of this study. WZ and GZ designed the methods. WZ carried them out and prepared the paper with contributions from all co-authors.

Competing interests

The authors declare that they have no conflict of interest.

References

Bond, T. C.: Spectral dependence of visible light absorption by carbonaceous particles emitted from coal combustion, Geophys. Res. Lett., 28, 4075-4078, 10.1029/2001gl013652, 2001.

Bond, T. C., Streets, D. G., Yarber, K. F., Nelson, S. M., Woo, J. H., and Klimont, Z.: A technology-based global inventory of black and organic carbon emissions from combustion, J. Geophys. Res.-Atmos., 109, 43, 10.1029/2003jd003697, 2004.

Bond, T. C., and Bergstrom, R. W.: Light absorption by carbonaceous particles: An investigative review, Aerosol Science and Technology, 40, 27-67, 10.1080/02786820500421521, 2006.

Bond, T. C., Doherty, S. J., Fahey, D. W., Forster, P. M., Berntsen, T., DeAngelo, B. J., Flanner, M. G., Ghan, S., Karcher, B., Koch, D., Kinne, S., Kondo, Y., Quinn, P. K., Sarofim, M. C., Schultz, M. G., Schulz, M., Venkataraman, C., Zhang, H., Zhang, S., Bellouin, N., Guttikunda, S. K., Hopke, P. K., Jacobson, M. Z., Kaiser, J. W., Klimont, Z., Lohmann, U., Schwarz, J. P., Shindell, D., Storelvmo, T., Warren, S. G., and Zender, C. S.: Bounding the role of black carbon in the climate system: A scientific assessment, J. Geophys. Res.-Atmos., 118, 5380-5552, 10.1002/jgrd.50171, 2013.

Castagna, J., Calvello, M., Esposito, F., and Pavese, G.: Analysis of equivalent black carbon multi-year data at an oil pre-treatment plant: Integration with satellite data to identify black carbon transboundary sources, Remote Sens. Environ., 235, 10, 10.1016/j.rse.2019.111429, 2019.

Chow, J. C., Watson, J. G., Crow, D., Lowenthal, D. H., and Merrifield, T.: Comparison of IMPROVE and NIOSH Carbon Measurements, Aerosol Science and Technology, 34, 23-34, 10.1080/02786820119073, 2001.

DeCarlo, P. F., Slowik, J. G., Worsnop, D. R., Davidovits, P., and Jimenez, J. L.: Particle morphology and density characterization by combined mobility and aerodynamic diameter measurements. Part 1: Theory (vol 38, pg 1185, 2004), Aerosol Science and Technology, 39, 184-184, 10.1080/02786820590928897, 2005.

Drinovec, L., Mocnik, G., Zotter, P., Prevot, A. S. H., Ruckstuhl, C., Coz, E., Rupakheti, M., Sciare, J., Muller, T., Wiedensohler,

A., and Hansen, A. D. A.: The "dual-spot" Aethalometer: an improved measurement of aerosol black carbon with real-time loading compensation, Atmospheric Measurement Techniques, 8, 1965-1979, 10.5194/amt-8-1965-2015, 2015.

Guo, Y. H.: Carbonaceous aerosol composition over northern China in spring 2012, Environmental Science and Pollution Research, 22, 10839-10849, 10.1007/s11356-015-4299-8, 2015.

Hansen, A. D. A., Rosen, H., and Novakov, T.: The aethalometer - an instrument for the real-time measurement of optical-absorption by aerosol-particles, Sci. Total Environ., 36, 191-196, 10.1016/0048-9697(84)90265-1, 1984.

Helin, A., Niemi, J. V., Virkkula, A., Pirjola, L., Teinila, K., Backman, J., Aurela, M., Saarikoski, S., Ronkko, T., Asmi, E., and Timonen, H.: Characteristics and source apportionment of black carbon in the Helsinki metropolitan area, Finland, Atmospheric Environment, 190, 87-98, 10.1016/j.atmosenv.2018.07.022, 2018.

Highwood, E. J., and Kinnersley, R. P.: When smoke gets in our eyes: The multiple impacts of atmospheric black carbon on climate, air quality and health, Environment International, 32, 560-566, 10.1016/j.envint.2005.12.003, 2006.

Johnson, T. J., Irwin, M., Symonds, J. P. R., Olfert, J. S., and Boies, A. M.: Measuring aerosol size distributions with the aerodynamic aerosol classifier, Aerosol Science and Technology, 52, 655-665, 10.1080/02786826.2018.1440063, 2018.

Karlsson, M. N. A., and Martinsson, B. G.: Methods to measure and predict the transfer function size dependence of individual DMAs, Journal of Aerosol Science, 34, 603-625, 10.1016/s0021-8502(03)00020-x, 2003.

Kim, J. H., Mulholland, G. W., Kukuck, S. R., and Pui, D. Y. H.: Slip correction measurements of certified PSL nanoparticles using a nanometer differential mobility analyzer (nano-DMA) for Knudsen number from 0.5 to 83, J. Res. Natl. Inst. Stand. Technol., 110, 31-54, 10.6028/jres.110.005, 2005.

Knutson, E. O., and Whitby, K. T.: Aerosol classification by electric mobility: apparatus, theory, and applications, Journal of Aerosol Science, 6, 443-451, https://doi.org/10.1016/0021-8502(75)90060-9, 1975.

Liu, C., Chung, C. E., Yin, Y., and Schnaiter, M.: The absorption Angstrom exponent of black carbon: from numerical aspects, Atmospheric Chemistry and Physics, 18, 6259-6273, 10.5194/acp-18-6259-2018, 2018.

Liu, D., Flynn, M., Gysel, M., Targino, A., Crawford, I., Bower, K., Choularton, T., Juranyi, Z., Steinbacher, M., Huglin, C., Curtius, J., Kampus, M., Petzold, A., Weingartner, E., Baltensperger, U., and Coe, H.: Single particle characterization of black carbon aerosols at a tropospheric alpine site in Switzerland, Atmospheric Chemistry and Physics, 10, 7389-7407, 10.5194/acp-10-7389-2010, 2010.

Matsui, H., Hamilton, D. S., and Mahowald, N. M.: Black carbon radiative effects highly sensitive to emitted particle size when resolving mixing-state diversity, Nature Communications, 9, 10.1038/s41467-018-05635-1, 2018.

Moosmuller, H., Chakrabarty, R. K., and Arnott, W. P.: Aerosol light absorption and its measurement: A review, Journal of Quantitative Spectroscopy & Radiative Transfer, 110, 844-878, 10.1016/j.jqsrt.2009.02.035, 2009.

Ning, Z., Chan, K. L., Wong, K. C., Westerdahl, D., Mocnik, G., Zhou, J. H., and Cheung, C. S.: Black carbon mass size distributions of diesel exhaust and urban aerosols measured using differential mobility analyzer in tandem with Aethalometer, Atmospheric

Environment, 80, 31-40, 10.1016/j.atmosenv.2013.07.037, 2013.

Onasch, T. B., Trimborn, A., Fortner, E. C., Jayne, J. T., Kok, G. L., Williams, L. R., Davidovits, P., and Worsnop, D. R.: Soot Particle Aerosol Mass Spectrometer: Development, Validation, and Initial Application, Aerosol Science and Technology, 46, 804-817, 10.1080/02786826.2012.663948, 2012.

Petzold, A., Ogren, J. A., Fiebig, M., Laj, P., Li, S. M., Baltensperger, U., Holzer-Popp, T., Kinne, S., Pappalardo, G., Sugimoto, N., Wehrli, C., Wiedensohler, A., and Zhang, X. Y.: Recommendations for reporting "black carbon" measurements, Atmospheric Chemistry and Physics, 13, 8365-8379, 10.5194/acp-13-8365-2013, 2013.

Ramachandran, S., and Rajesh, T. A.: Black carbon aerosol mass concentrations over Ahmedabad, an urban location in western India: Comparison with urban sites in Asia, Europe, Canada, and the United States, J. Geophys. Res.-Atmos., 112, 19, 10.1029/2006jd007488, 2007.

Ran, L., Deng, Z. Z., Wang, P. C., and Xia, X. A.: Black carbon and wavelength-dependent aerosol absorption in the North China Plain based on two-year aethalometer measurements, Atmospheric Environment, 142, 132-144, 10.1016/j.atmosenv.2016.07.014, 2016.

Schwarz, J. P., Gao, R. S., Fahey, D. W., Thomson, D. S., Watts, L. A., Wilson, J. C., Reeves, J. M., Darbeheshti, M., Baumgardner, D. G., Kok, G. L., Chung, S. H., Schulz, M., Hendricks, J., Lauer, A., Karcher, B., Slowik, J. G., Rosenlof, K. H., Thompson, T. L., Langford, A. O., Loewenstein, M., and Aikin, K. C.: Single-particle measurements of midlatitude black carbon and light-scattering aerosols from the boundary layer to the lower stratosphere, J. Geophys. Res.-Atmos., 111, 15, 10.1029/2006jd007076, 2006.

Schwarz, J. P., Spackman, J. R., Fahey, D. W., Gao, R. S., Lohmann, U., Stier, P., Watts, L. A., Thomson, D. S., Lack, D. A., Pfister, L., Mahoney, M. J., Baumgardner, D., Wilson, J. C., and Reeves, J. M.: Coatings and their enhancement of black carbon light absorption in the tropical atmosphere, J. Geophys. Res.-Atmos., 113, 10, 10.1029/2007jd009042, 2008.

Soto-Garcia, L. L., Andreae, M. O., Andreae, T. W., Artaxo, P., Maenhaut, W., Kirchstetter, T., Novakov, T., Chow, J. C., and Mayol-Bracero, O. L.: Evaluation of the carbon content of aerosols from the burning of biomass in the Brazilian Amazon using thermal, optical and thermal-optical analysis methods, Atmospheric Chemistry and Physics, 11, 4425-4444, 10.5194/acp-11-4425-2011, 2011.

Tavakoli, F., and Olfert, J. S.: An Instrument for the Classification of Aerosols by Particle Relaxation Time: Theoretical Models of the Aerodynamic Aerosol Classifier, Aerosol Science and Technology, 47, 916-926, 10.1080/02786826.2013.802761, 2013.

Taylor, J. W., Allan, J. D., Liu, D., Flynn, M., Weber, R., Zhang, X., Lefer, B. L., Grossberg, N., Flynn, J., and Coe, H.: Assessment of the sensitivity of core / shell parameters derived using the single-particle soot photometer to density and refractive index, Atmos. Meas. Tech., 8, 1701-1718, 10.5194/amt-8-1701-2015, 2015.

Tunved, P., Cremer, R. S., Zieger, P., and Strom, J.: Using correlations between observed equivalent black carbon and aerosol size distribution to derive size resolved BC mass concentration: a method applied on long-term observations performed at Zeppelin station, Ny-Alesund, Svalbard, Tellus Ser. B-Chem. Phys. Meteorol., 73, 1-17, 10.1080/16000889.2021.1933775, 2021.

Viidanoja, J., Kerminen, V.-M., and Hillamo, R.: Measuring the Size Distribution of Atmospheric Organic and Black Carbon Using

Impactor Sampling Coupled with Thermal Carbon Analysis: Method Development and Uncertainties, Aerosol Science and Technology, 36, 607-616, 10.1080/02786820252883847, 2002.

Wang, J. D., Wang, S. X., Wang, J. P., Hua, Y., Liu, C., Cai, J., Xu, Q. C., Xu, X. T., Jiang, S. Y., Zheng, G. J., Jiang, J. K., Cai, R. L., Zhou, W., Chen, G. Z., Jin, Y. Z., Zhang, Q., and Hao, J. M.: Significant Contribution of Coarse Black Carbon Particles to Light Absorption in North China Plain, Environ. Sci. Technol. Lett., 9, 134-139, 10.1021/acs.estlett.1c00953, 2022.

Yu, H., Wu, C., Wu, D., and Yu, J. Z.: Size distributions of elemental carbon and its contribution to light extinction in urban and rural locations in the pearl river delta region, China, Atmospheric Chemistry and Physics, 10, 5107-5119, 10.5194/acp-10-5107-2010, 2010.

Zhang, R. Y., Khalizov, A. F., Pagels, J., Zhang, D., Xue, H. X., and McMurry, P. H.: Variability in morphology, hygroscopicity, and optical properties of soot aerosols during atmospheric processing, Proceedings of the National Academy of Sciences of the United States of America, 105, 10291-10296, 10.1073/pnas.0804860105, 2008.

Zhao, G., Tao, J. C., Kuang, Y., Shen, C. Y., Yu, Y. L., and Zhao, C. S.: Role of black carbon mass size distribution in the direct aerosol radiative forcing, Atmospheric Chemistry and Physics, 19, 13175-13188, 10.5194/acp-19-13175-2019, 2019.

Zhao, G., Shen, C. Y., and Zhao, C. S.: Technical note: Mismeasurement of the core-shell structure of black carbon-containing ambient aerosols by SP2 measurements, Atmospheric Environment, 243, 10.1016/j.atmosenv.2020.117885, 2020a.

Zhao, G., Yu, Y., Tian, P., Li, J., Guo, S., and Zhao, C.: Evaluation and Correction of the Ambient Particle Spectral Light Absorption Measured Using a Filter-based Aethalometer, Aerosol and Air Quality Research, 20, 10.4209/aaqr.2019.10.0500, 2020b.

Zhao, G., Tan, T. Y., Zhu, Y. S., Hu, M., and Zhao, C. S.: Method to quantify black carbon aerosol light absorption enhancement with a mixing state index, Atmospheric Chemistry and Physics, 21, 18055-18063, 10.5194/acp-21-18055-2021, 2021a.

Zhao, W. L., Tan, W. S., Zhao, G., Shen, C. Y., Yu, Y. L., and Zhao, C. S.: Determination of equivalent black carbon mass concentration from aerosol light absorption using variable mass absorption cross section, Atmospheric Measurement Techniques, 14, 1319-1331, 10.5194/amt-14-1319-2021, 2021b.

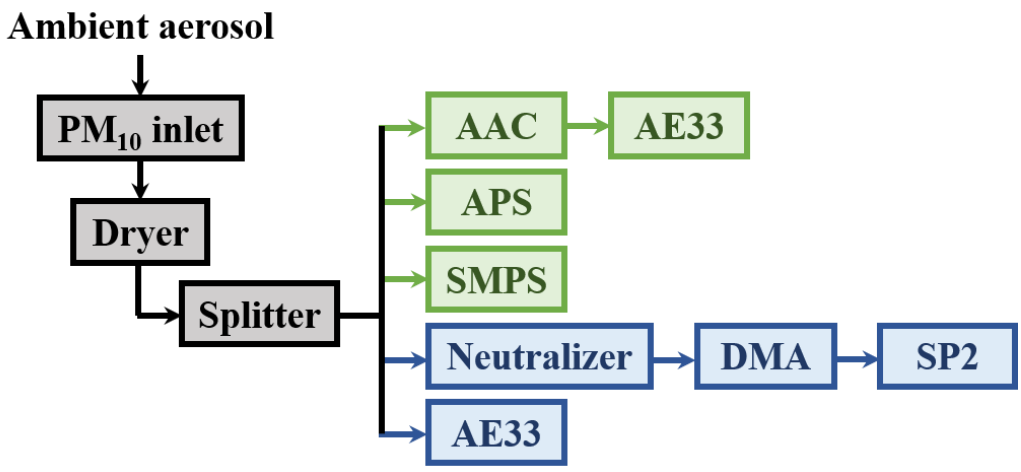

Figure 1: Schematic diagram of the measurement (green) and the validation (blue) setup.

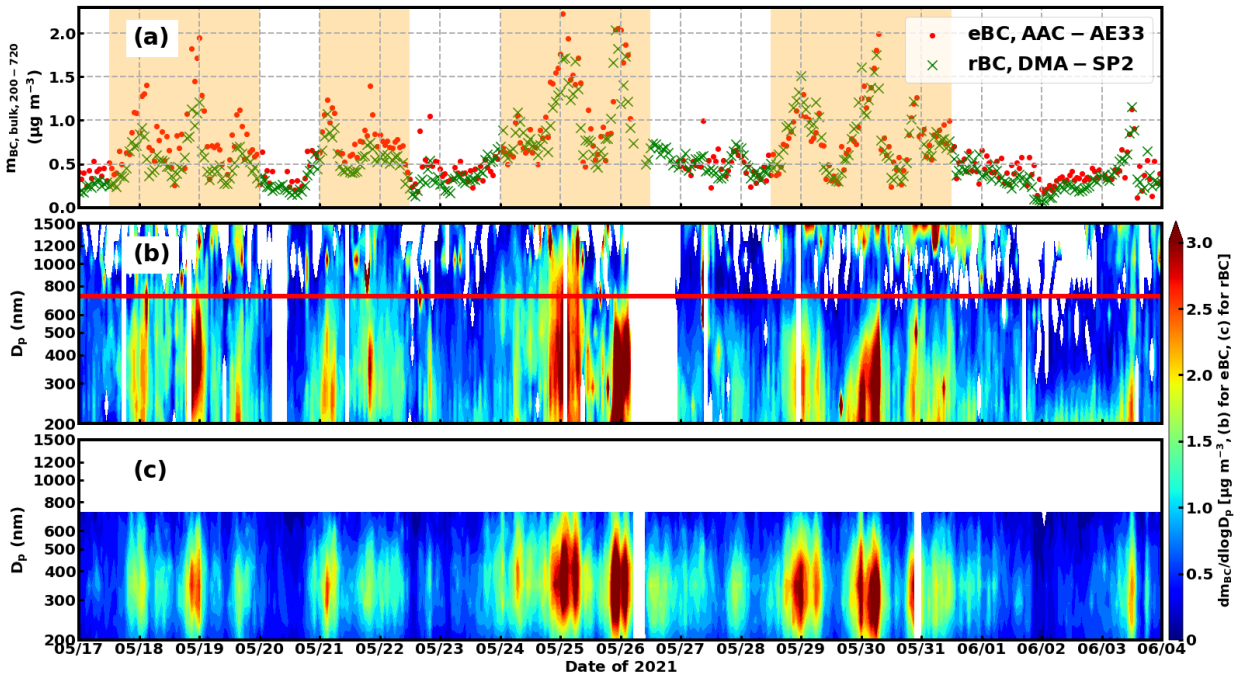

Figure 2: Time series of (a) $m_{BC,bulk}$ from BCMSD integrated from 200 nm to 720 nm ($m_{BC,bulk,200-720}$) determined by the proposed method (red dot, denoted as "eBC, AAC – AE33") and DMA – SP2 (green cross, denoted as "rBC, DMA – SP2"), BCMSD determined by (b) the proposed method (eBC) and (c) DMA – SP2 (rBC). The red line in (b) marked particle size of 720 nm. The pollution episodes were shaded with orange in (a).

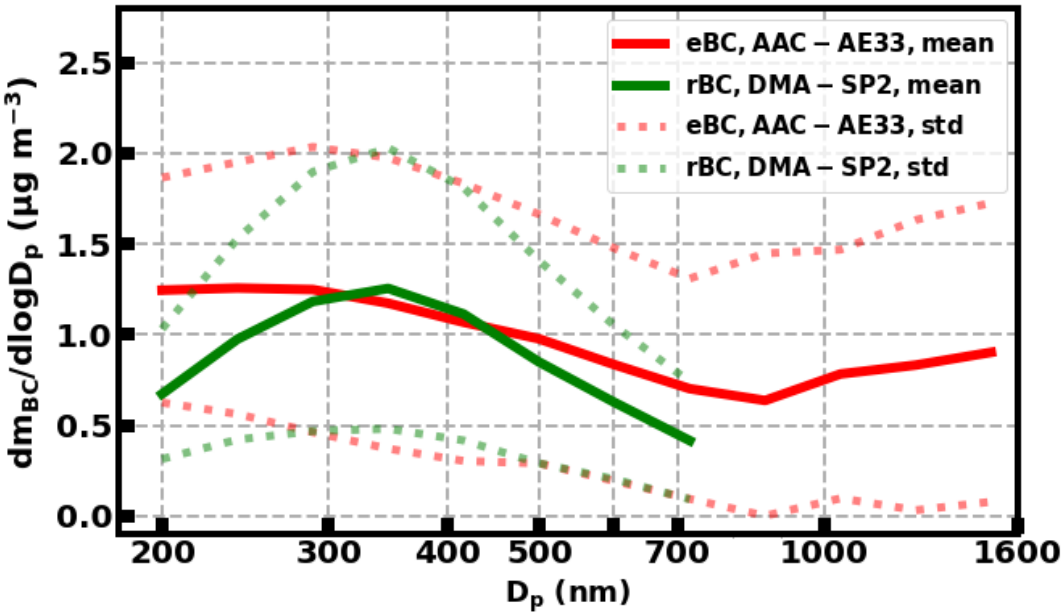

Figure 3: Mean and std of $eBCMSD_{AAC-AE33}$ (green) and $rBCMSD_{DMA-SP2}$ (red) during the measurement period. Mean BCMSD was denoted by the solid line. Std of BCMSD was denoted by the dotted line.

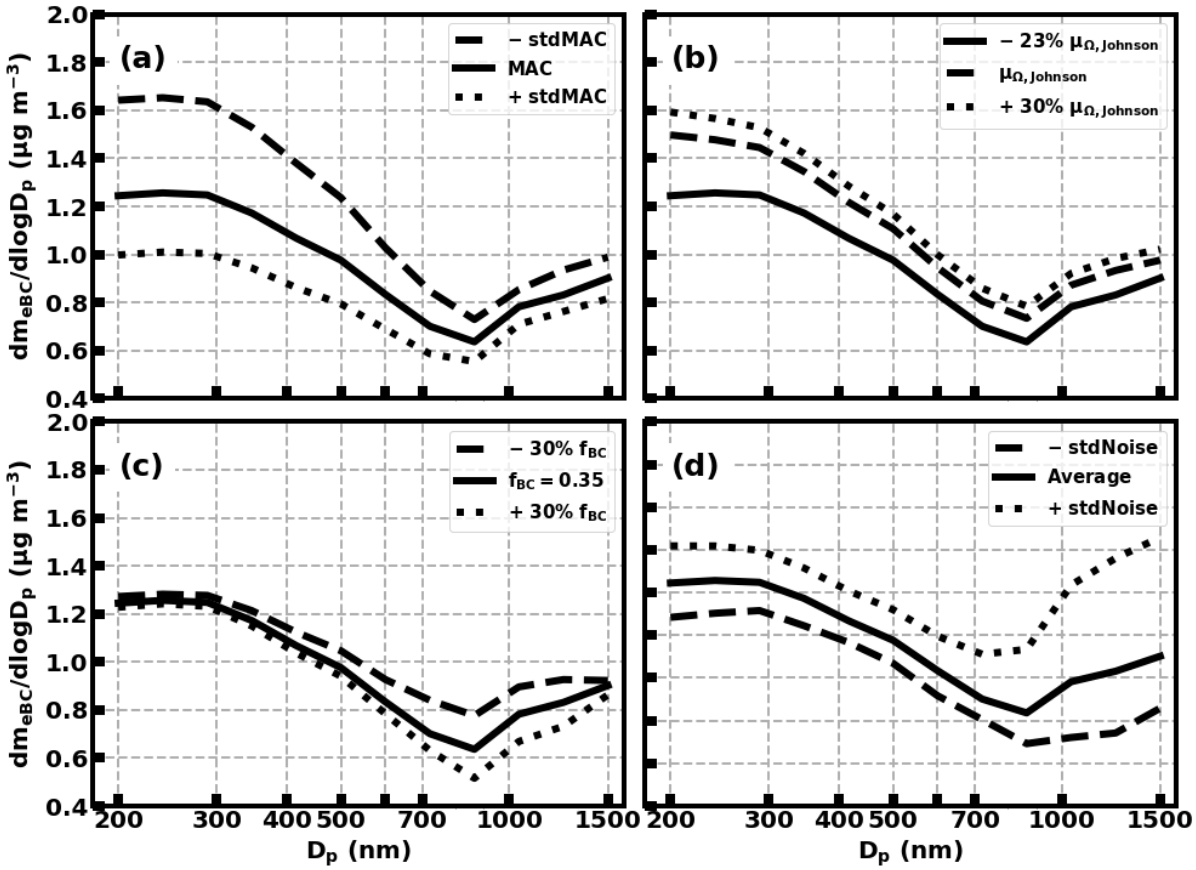

Figure 4: Uncertainty in eBCMSD$_{AAC\text{-}AE33}$ arising from (a) MAC lookup table, (b) transfer function inversion, (c) f_{BC} and (d) instrumental noise. The solid lines in each panel were the same and were the mean eBCMSD$_{AAC\text{-}AE33}$ during the measurement period. The dotted lines and dashed lines in each panel were mean eBCMSD$_{AAC\text{-}AE33}$ ± standard deviation (std) calculated from (a) MAC + std of MAC and MAC – std of MAC, (b) $\mu_{\Omega,Johnson}$ and 1.3 times $\mu_{\Omega,Johnson}$, (c) f_{BC} of 35% times 0.7 and 1.3, (d) eBCMSD$_{AAC\text{-}AE33}$ + std of instrumental noise and – std of instrumental noise.

Table 1: The Uncertainty in the $m_{eBC,bulk,AAC\text{-}AE33,200\text{-}720}$ resulted from MAC lookup table, transfer function inversion, f_{BC} and instrumental noise.

Uncertainty source	MAC	Transfer function inversion	f_{BC}	Instrumental noise
Uncertainty	– 20 % ~ + 28 %	– 1 % ~ + 21 %	– 3 % ~ + 3 %	– 2 % ~ – 1 %